

# Hyperspectral Plasmonics

Dominic Lepage, Alvaro Jiménez and Jan J. Dubowski\*

Interdisciplinary Institute for Technological Innovation (3IT)  
Université de Sherbrooke, Sherbrooke, Québec J1K 2R1, Canada

## ABSTRACT

We investigate the functioning of a monolithically integrated surface plasmon resonance (SPR) device comprising a metal coated dielectric layer deposited atop a luminescence emitting quantum well (QW) wafer. The device takes advantage of the uncollimated and incoherent emission of QWs. The light modulations in the far field, where the surface plasmons are extracted by a grating, have been calculated for a continuum of energies and wavevectors injected by the substrate. We discuss the results of our calculations based on a tensorial rigorous coupled-wave analysis aimed at the full description of SPR coupling in QW semiconductor-based architectures, designed for biosensing applications. The surface roughness induced by various nanofabrication methods is also studied, given that it is one of the main limiting factors in diffraction-based SPR sensing. This aspect is studied for thin film microstructures operating in the visible and near-infrared spectral regions. The surface roughness and dielectric values for various deposition rates of very thin Au films are examined. We finally introduce a novel experimental method for direct mapping of the electromagnetic (EM) wave dispersion that enabled us monitoring of a massive amount of light-scattering related information. We present the results of far field measurements of the complete 3D dispersion relation of a SPR effect induced by this nanodevice. The quasi-real time method is applied for tracking SPR directly in the  $E(\mathbf{k})$  space. Those additional dimensions, measured with scalable tracking precision, reveal anisotropic surficial interactions and provide spectroscopic response for SPR.

**Keywords:** Surface plasmon resonance, optical devices, scattering, biosensing, hyperspectral imaging

## 1. INTRODUCTION

The intrinsic surficial sensitivity of the surface plasmon resonance (SPR) effect is a well known consequence of the spatial localization of the electromagnetic fields and charge coupled modes. The surface plasmons (SPs) can be employed as information carriers to monitor the optical changes occurring within their evanescent field, typically 100 to 200 nm from the metal surface. Multiple commercial and research apparatus exploit the advantageous properties of the SPR for biochemical analysis and imagery of processes localized on metal surfaces<sup>1</sup>.

Conventionally, SPR tracking consists in probing the dispersion relation  $E(\mathbf{k})$  of the charge coupled electromagnetic (EM) wave under a predetermined condition of resonance in either energy  $E$  (fixed incident energy) or in wavevector  $\mathbf{k}$  (fixed incident coupling angle). Time-resolvable biochemical adsorption events can then be monitored for that resonance energy or wavevector<sup>1,2</sup>. The same can be accomplished spatially for a given time using SPR imaging microscopy<sup>3,4</sup>. Tracking of a wavevector (i.e. incidence angle) is more frequently used for its practicality, a consequence of the laser technology capable of delivering collimated and high power beams of monochromatic light. Resonance monitoring in  $E$  or  $\mathbf{k}$  of SPs is often carried out under prism-based Kretschmann–Reather architecture for simplicity and efficiency, but it can result in a complex and bulky experimental setup<sup>1-4</sup>. A monolithically integrated SPR microchip, which could be advantageously inserted in specimen processing hardware for wholly automated analyses, has yet to be demonstrated. A first step towards this integration was the embedment of a light source in a nanostructure designed for SPR. Strong luminescence from bulk semiconductor materials or their nanostructures in form of thin films, quantum well (QW), quantum dot (QD), and arrays of nano-crystals (NCs) makes them attractive for the development of monolithically integrated SPR devices. With the goal of incorporating SPR technology into an automated specimen analysis system<sup>5</sup>, we propose an alternative method of achieving SPR consisting in the integration of semiconductor-based nanostructure. The resulting platform is capable of coupling a multiplexed SPR signal in both wavevectors  $\mathbf{k}$  and energies  $E$ , thus potentially yielding an enhanced picture of the surficial biochemical events.

---

\* [jan.j.dubowski@usherbrooke.ca](mailto:jan.j.dubowski@usherbrooke.ca); [www.dubowski.ca](http://www.dubowski.ca)

Therefore, rather than monitoring only one variable at a time for the resonance tracking, as in traditional systems, a more global approach would be to directly monitor the general dispersion relation of any light emitted or diffracted by the architecture. This would provide a complete map in  $I(E, \mathbf{k})$  under specific conditions, thus describing the whole system's state. In the specific case of SPs, their resonance occurs in a particular plane in the three-dimensional (3D) space of the intensity distribution of the  $E(\mathbf{k})$  dispersion. Nonetheless, the measurement of the complete dispersion relation is a devious experiment because of the fundamental intertwinement of the variables involved. Consequently, the full and simultaneous characterization of EM-waves has so far been impractical because of the difficulty to separate these variables and collect the volume of data that would thus be generated.

We have proposed a solution to this problem through the use of a hyperspectral imaging technology<sup>6,7</sup>. The resulting setup can measure and store the dispersion relation properties of any EM waves in quasi real-time with scalable resolution. We have applied this technology to carry out SPR analyses of our integrated quantum semiconductor devices, where the hyperspectral measurements are to be employed for biosensing.

## 2. SPR INDUCED BY UNCOLLIMATED AND BROADBAND LIGHT SOURCE

The SPR event takes place in the 3D space of the intensity distribution of the dispersion  $E(\mathbf{k})$ . It can be induced optically where an EM wave meets a metal-dielectric interface. At a given energy,  $E$ , the resonance is achieved when the projected in-plane wavevector of the incoming EM wave has a wavevector of norm  $k_{\parallel}^2 = k_x^2 + k_y^2 = k_{\text{SPR}}^2$ , as illustrated in Fig.1 a)<sup>2</sup>. This resonance can be met for various energies and values of  $k_{\text{SPR}}$ , following a SPR dispersion relation  $E(k_x, k_y)$  distributed in a 3D Fourier space, as caricatured in Fig.1 b). Measuring the time-dependent modulations of any point of such SPR surfaces is employed for high sensitivity tracking of the biochemical events occurring within the SPs evanescent EM fields.

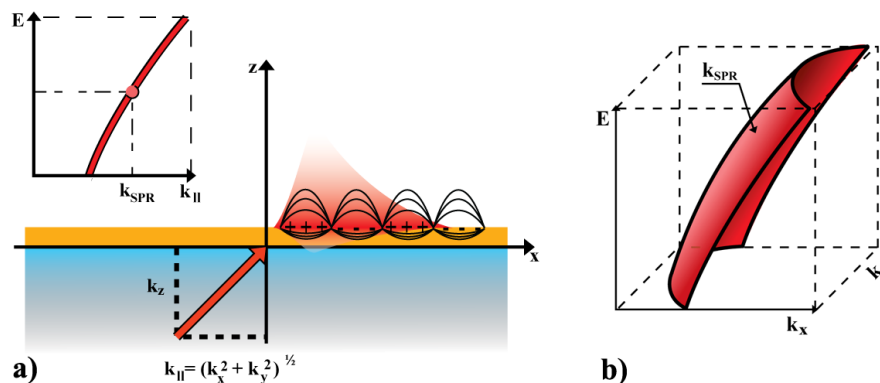


Figure 1. a) SPR tracking consists in probing the resonance phenomena across the dispersion relation  $E(\mathbf{k})$  of the charge coupled EM wave under fixed conditions in either energy,  $E$ , or in wavevector  $k_{\parallel}$ , function of the coupling angles. b) Under specific circumstances, SPR can be induced at any energies where  $k_{\parallel} = k_{\text{SPR}}(E)$ . The resulting surfaces in  $E(\mathbf{k})$  can be employed for high sensitivity spectro-angular SPR tracking.

A dielectric-metal-dielectric (DMD) nanostructure deposited on top of a luminescent semiconductor can also provide the conditions suitable for SPR formation and observation of a variety of bio-chemical reactions. Because of the proximity and the nature of the materials involved, the light injected in such a system is uncollimated and usually incoherent, as opposed to laser induced SPR. As illustrated in the inset of Fig. 2, any given point of a metallic layer in the DMD microstructure will be exposed to the whole wavevector spectrum  $k_{\parallel}$  (polar angles of emission) and couple all SPR modes possibly supported by the architecture for the excited energies. While a constant light intensity is measured at a given plane of the real-space  $(x, y)$ , every supported photonic mode is induced in the Fourier-space  $(k_{\parallel})$ . Fig. 3 illustrates this principle by showing the distribution of the P-polarized electric field intensity for a vertical cross section  $(z)$  of such architecture at the various wavevectors  $(k_{\parallel})$  emitted by an embedded QW. The employed method of calculation for the distribution of the electric field intensity, as shown in Fig. 3, is detailed in the following sections. The embedded semiconductor light sources will have a relatively large emission spectra (from  $\pm 50\text{nm}$  in QW to  $\pm 100\text{nm}$  in NCs), they will thus simultaneously generate a continuum of SPs dispersion relation  $E(k_{\parallel})$ , i.e. the whole surface of

Fig.1 b). This case is different from the traditional “macro” SPs coupling, where one energy is considered and one wavevector is injected by the irradiating laser <sup>1,2</sup>.

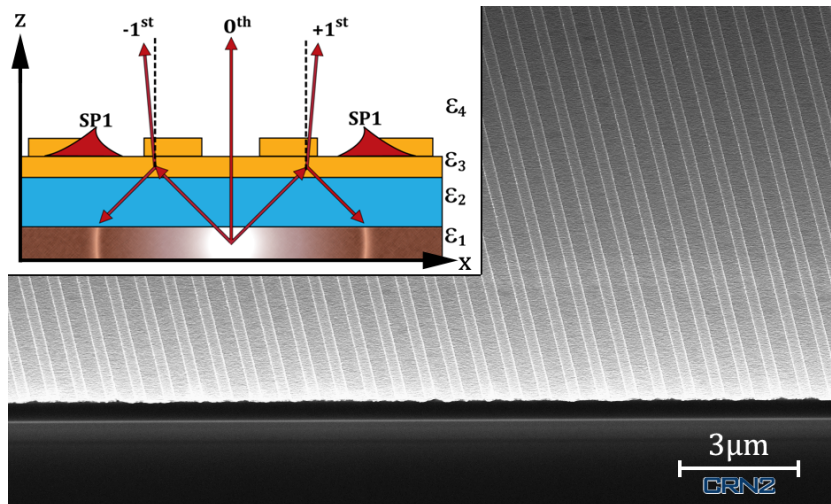


Figure 2. (main) A scanning electron microscope (SEM) image of the architecture comprising an embedded QW structure, an adaptative layer of dielectric and a gold interface with air. (insert) The embedded semiconductor ( $\epsilon_1$ ) emits an uncollimated and usually incoherent light. At a fixed energy, the DMD interface ( $\epsilon_2 - \epsilon_3 - \epsilon_4$ ) is exposed to a continuous range of wavevector excitations taking place in the Fourier space ( $k_{||}$ ) and coupling all the photonic modes supported by the architecture. If the light source emits a broad energy spectrum, a continuum of the dispersion relations  $E(\mathbf{k}_{||})$  can be met <sup>6</sup>.

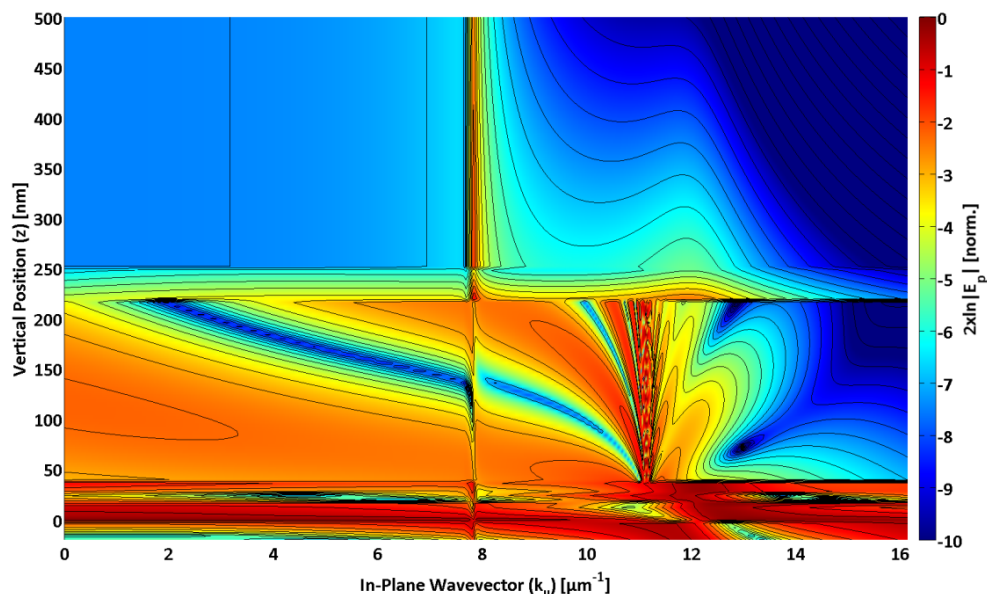


Figure 3. Distribution of the P-polarized electric field intensity in logarithmic scale for various vertical positions of the architecture ( $z$ ) in the near field at various emitted in-plane wavevectors ( $k_{||}$ ) for  $E=1.51\text{eV}$  light emissions. The architecture is a GaAs-AlGaAs QW heterostructure with a  $\text{SiO}_2$ -Au-Air DMD as presented in previous work <sup>6,7</sup>. Note the two SPR events occurring concurrently (past their respective TIR) <sup>12</sup>.

As shown in Fig.2, a one-dimensional grating is fabricated atop the metallic layer to diffract the coupled SPs within the measurable light cone at the  $\pm 1^{\text{st}}$  diffraction orders. The architecture of this integrated and self aligned SPR system has also the advantage of coupling two SPR modes, one of which can be used as a signal normalization reference <sup>7, 12</sup> (not shown in Fig. 2, but visible in Fig. 3). The signal to noise ratio (S/N) of coupling in the  $0^{\text{th}}$  diffraction order was found to increase hundred fold compared to the diffraction assisted SPR coupling. The uncollimated and broadband SPR coupling in such systems implies that the measurement of the dispersion relation of the coupled SPs, traceable in both E and k, would require a highly efficient SPR imaging technique.

### 3. NANOFABRICATION AND SURFACE ROUGHNESS

The main limitation of monitoring diffracted SPs, as a mean to biodiagnostic, is the intensity of the diffracted SPs in the far field. For a given luminous flux from the source, the grating shape and the SPs propagation distance will contribute the most to the output quality of the signal. The SPs propagation distance,  $\Lambda_{\text{SP}}$ , will be influenced by thermal loss from the metal dampening.  $\Lambda_{\text{SP}}$  will also be limited by scattering on the grating and on the surface roughness. Additional losses will occur through radiations in thin films, illustrated by a larger SPs complex wave vectors due to coupling to the other interface (known as Fano modes) <sup>8</sup>. To maximize the SPs diffraction, and thus the measured signal, one must minimize all the other factors.

The surface roughness is known to play a very important role in the limitation of the SPs propagation distances, as the corrugation will diffract a fraction of the SPs light flux. Indeed, the mean free path of the SPs wave has been found to be inversely proportional to the square of the surface roughness height, for a given SP energy and fixed metal dielectric (the complete formulation is available in literature <sup>9</sup>). To reduce the surface roughness to a minimum during the fabrication process of the architectures, we analyzed different materials and deposition techniques <sup>10</sup>. The substrate layer on which the metallic layer is going to be deposited is the first concern, as its roughness directly impacts the quality of the subsequent thin films. Fig. 4 presents the surface roughness, measured by ellipsometry for three dielectrics, SiO<sub>2</sub>, Si<sub>3</sub>N<sub>4</sub> and polymethyl methacrylate (PMMA), commonly employed in nanofabrication.

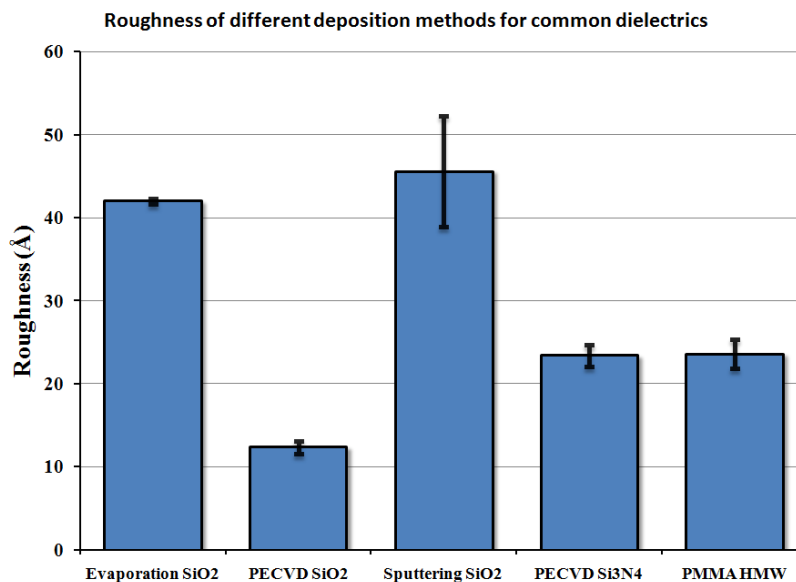


Figure 4. Surface roughness for various dielectric materials and fabrication methods; SiO<sub>2</sub> is explored using e-beam evaporation, plasma sputtering and plasma enhanced chemical vapour deposition (PECVD). Si<sub>3</sub>N<sub>4</sub> is an interesting material due to its relatively large dielectric constant, and is deposited through PECVD. The spin coating of a common electro resist, PMMA, is also presented. On average, 300nm of SiO<sub>2</sub> or Si<sub>3</sub>N<sub>4</sub> and 150nm of PMMA were deposited atop Si substrates. Uncertainties represent the standard variation between three independent material depositions <sup>10</sup>.

Fig.4 shows that SiO<sub>2</sub> deposited through PECVD is the best candidate for thin films in the present case, with a consistent surface roughness of 12.3±0.8 Å. The energy dependent dielectric values for the resulting layers have also been measured by ellipsometry and presented elsewhere<sup>10</sup>.

The subsequent layer for the structure in Fig. 2 consists in a continuous thin film of Au atop of which a grating region is constructed for the SPs extraction. Again, the surface roughness of Au is studied, this time only for the e-beam evaporation technique (using a BOC Edwards evaporator model Auto 306) for various deposition rates. The target thickness for the Au layers is 20nm. Fig. 5 presents the surface roughness for the various deposition rates. In depth SEM analyses have shown that for small deposition rates (≤ 1Å/s), Au nanodroplets tend to cool down and form 100-200 nm wide clusters, thus yielding a relatively high surface roughness. On the other hand, for large deposition rates (> 3Å/s), the Au grains remain small (~6nm) and are very compact on the surface. However, very large Au pieces, up to about 1µm<sup>2</sup>, are found in this case on the surface. Examples of these two behaviours are presented in Fig. 6. As shown in Fig. 5, a relatively slow deposition rate, at around 1Å/s, presents tradeoffs of the two regimes and seems to be the ideal case for deposition of low-roughness Au films. We calculated the SPs propagation length to be  $\Lambda_{SP} = 5.22 \pm 0.02 \mu\text{m}$  on the 20nm Au layer (with  $\epsilon_{Au} = -31.2071 + 3.5632i$ )<sup>11</sup>.

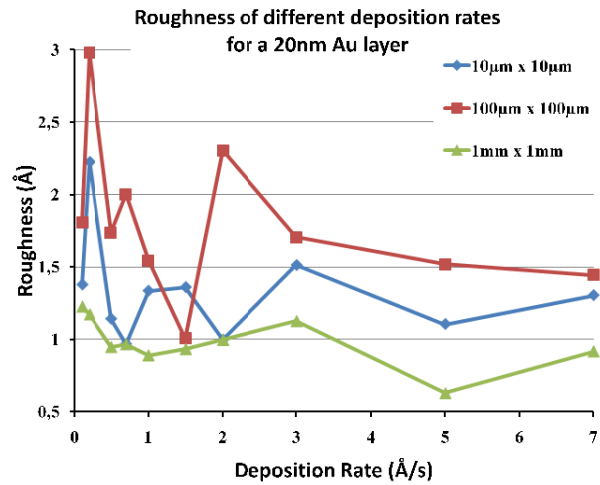


Figure 5. Surface roughness for various e-beam deposition rates of Au; Various sampling areas were examined: the 10 and 100 µm<sup>2</sup> regions are measured by AFM while the 1mm<sup>2</sup> region is the roughness yielded by ellipsometry<sup>10</sup>.

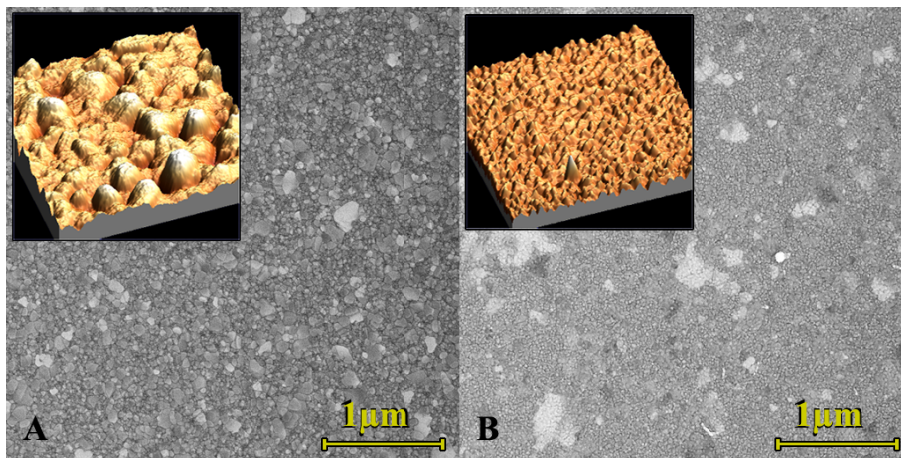


Figure 6. SEM images of surface roughness for Au surfaces; as presented in literature<sup>10</sup> for A) 0.2 Å/s deposition rate. The roughness is high and but relatively homogeneous over the surface. Au grains are clustering over the surface and present a lower density. The insert is a 10µm<sup>2</sup> AFM profile. B) At 0.7 Å/s deposition rate, the localised surface roughness is smaller, more compact and a lower clusterization with the typical grain size of Au at 6nm.

#### 4. CALCULATIONS

The optimization of the structures and the far field emissions of the QW-SPR nanostructure are analytically calculated using a tensorial version of Rigorous Coupled-Wave Analysis (RCWA). No approximations are used for material properties or for the grating geometry. The method allowed us to predict the coupling of semiconductor photoluminescence (PL) to SPs generating architectures and describe the propagation of SPs in both the near- and far-fields. The TRCWA approach was preferred in these cases because it has been shown to be remarkably robust: for arbitrary shapes, it is able to reliably compute the electromagnetic field distribution for any wavelengths and incidence

angles<sup>13-15</sup>. For a given architecture, a set of variables, such as energies, angles, spatial positions or dielectric thicknesses are solved simultaneously through tensor algebra. A 2D or 3D slice of the solution, such as near-field spatial distribution or a dispersion relation map  $E(\mathbf{k}_{||})$ , can then be presented in the form of a plot. This tensorial approach generates an efficient design tool to address specific targets in photonic or biochemical responses as well as the optimization of existing architectures. Any layered architecture can be calculated with multiple parameters, but here we present the results addressing a specific design shown in Fig. 2, where a 20nm Au ( $\epsilon_3$ ) layer is deposited atop 472nm of SiO<sub>2</sub> ( $\epsilon_2$ ) on a GaAs-AlGaAs QW structure ( $\epsilon_1$ ). Atop this structure, we build a 750nm period (P) Au grating, 20nm in height and of a ridge to groove ratio of 0.4. The grating covers 1mm<sup>2</sup> of the substrate and is thus considered quasi infinite since  $\Lambda_{SP} \ll 1\text{mm}$ . Measurements are carried out in air ( $\epsilon_4$ ) at room temperature. This specific device was designed to couple SPs from the 0<sup>th</sup> diffraction order for all the energies emitted by its QW microstructure. Diffraction at the  $\pm 1^{\text{st}}$  order occurs on the grating with the SPs propagation through the corrugated grating layer. All the diffraction orders occurring within the structure are taken into account in the calculations, but really become negligible in intensity after the  $\pm 2^{\text{nd}}$  diffraction orders.

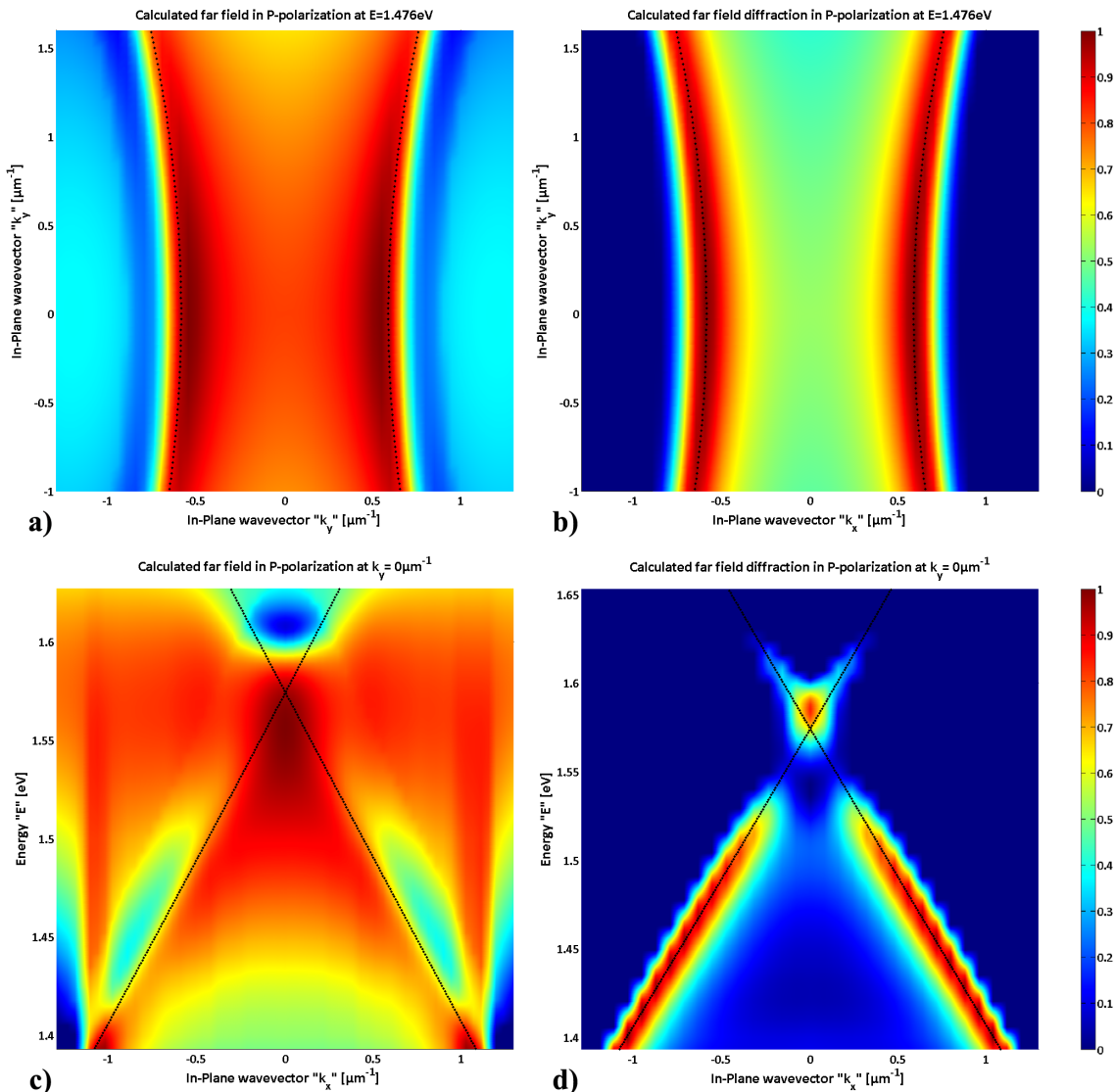


Figure 7 a) Calculated intensity dispersion in  $I(k_x, k_y)$  for the architecture presented in Fig.2 and a fixed energy of 1.476 eV. The dominant maxima are induced by the in-plane SPs, which are coupled at the 0<sup>th</sup> order between the Au and Air layer, diffracted by the unidimensional grating, as illustrated in Fig.7 b). The black lines are tracking the SPR maxima in  $\mathbf{k}$ . Fig.7 c) shows a cross section at  $k_y=0$  of the  $I(E, k_x)$ , for various energies emitted by the QW structure. Fig.7 d) illustrates how the main SP features are diffracted in the  $\pm 1^{\text{st}}$  orders. Again, the black lines are following the local maxima from SPR at different energies<sup>6</sup>.

Fig.7 a) presents the predicted  $k_x$ - $k_y$  wavevector map in the far field at  $E=1.476$  eV. Here, the P-polarization (TM) is presented, along with the  $0^{\text{th}}$ ,  $\pm 1^{\text{st}}$  and  $\pm 2^{\text{nd}}$  diffraction orders. The transmission of the S-polarization (TE) is not shown as it presents no important intensity modulations in  $\mathbf{k}$  and no surficial dependent features. It therefore shifts the intensity modulations by a flat component. The resonance of the SPs is the dominant feature in Fig.7 a), as illustrated in Fig.7 b) where only the contribution coming from the  $\pm 1^{\text{st}}$  diffraction orders is shown. The conical diffraction of the one-dimensional grating extract the SPs where  $\mathbf{k}_\parallel = \mathbf{k}_{\text{SPR}} \pm n \mathbf{k}_G$ , with  $n \in \mathbb{Z}$ ,  $\mathbf{k}_G = 2\pi/P \hat{\mathbf{x}}$ , and  $|\mathbf{k}_x + \mathbf{k}_y| = |\mathbf{k}_{\text{SPR}}|$ . Tracking the modulations of the SPR in  $k_x$ - $k_y$  space provides a two dimensional surface sensitive method of monitoring biochemical interactions with increased sensitivity<sup>16, 17</sup>. The black lines represent the peaks of the diffracted SPs resonance for  $E=1.476$  eV. Fig.7 c) now presents a different cut of the calculated far field dispersion  $I(E, k_x, k_y)$  emitted by the architecture of Fig. 2, at fixed in-plane wavevector  $k_y=0$ . The results are shown for P-polarized light and for all diffraction orders. Again, the main features come from the diffraction in the  $\pm 1^{\text{st}}$  order of the SPR, as isolated in Fig.7 d) where only the  $\pm 1^{\text{st}}$  diffraction orders are shown. The modulations in energy ( $E$ ) from the QW PL are not applied for clarity. Here, a projection on  $k_y=0$  of the dispersion relation  $E(\mathbf{k})$  of the coupled SPs is visible. The slopes of the lines correspond to the group velocity of SPs propagating in  $\pm \hat{\mathbf{x}}$  directions. Monitoring the modulations in  $E(\mathbf{k})$  provides spectral information on surficial events in the SPs near field. The black lines are the local maxima corresponding to diffracted SPs for various  $E(\mathbf{k})$ . One should notice that 2-dimensional projections of light intensities are convenient for demonstration purposes, but the dispersion relations are in fact multidimensional. Thus, the calculations and measurements are actually cubes of light intensities dispersion, where surfaces in  $I(E, k_x, k_y)$  represent the SPs state at the architecture's surface. Tracking the time-dependent displacement of those surfaces, as biochemical events take place on the surface of an integrated QW-SPR device, will provide a large amount of data, the equivalent of *up to*  $10^8$  traditional SPR experiments carried concurrently<sup>1, 2</sup>. The challenging task to experimentally track the resonance in the  $I(E, k_x, k_y)$  space, requires an innovative measuring approach, such as that offered by the hyperspectral imaging technology.

## 5. HYPERSPECTRAL MEASUREMENTS

There are several advantages in monitoring self-induced SPR through uncollimated emissions, when compared to traditional SPR techniques. For instance, many SPR modes can be coupled simultaneously, generating intrinsic references to the measurements<sup>7, 12, 18</sup>. Moreover, the monolithic integration with semiconductor technology generates a self-aligned, self-referred, ultra-compact and potentially inexpensive SPR platform. When using broadband coupling, as with QW or NCs semiconductor microstructures, SPR can be monitored over ranges of energies for various excitation angles concurrently: generating a full spectroscopic SPR platform.

Hyperspectral imaging technology has been growing in applications for the past decade, where the main fields of interests were found in astronomy, surveillance and crop monitoring. The basic idea is to spectrally ( $E$ ) spread a 2D map (ex:  $x$ - $y$ ) into a 3D cube with intensity distribution  $I(E, x, y)$ . Each resulting pixel of the image now has a full energy spectrum associated with it. We have recently implemented a hyperspectral imaging PL mapping (HI-PLM) instrument to analyze PL of quantum semiconductor microstructures during the functionalization of their surfaces with different molecules<sup>19, 20</sup>. Room temperature measurements of  $I(E, x, y)$  from up to  $1\text{cm}^2$  samples could be completed with this instrument in 1 to 10 minutes depending on the spectral and spatial resolution.

We have modified such HI-PLM system to resolve, instead of the  $x$ - $y$  space, the wavevectors space  $k_x$ - $k_y$  of the light emissions entering the system. The result is a hyperspectral mapping in 3D of the dispersion relation of the emitted light in  $I(E, k_x, k_y)$ . A specific and direct application of this instrument is the mapping of the dispersion of the light emitted by a quantum semiconductor SPR architecture<sup>6, 7</sup>, including the diffraction of SPs in energy and wavevectors. Fig. 8 presents the basic schematics of the hyperspectral instrument applied for this purpose<sup>6</sup>.

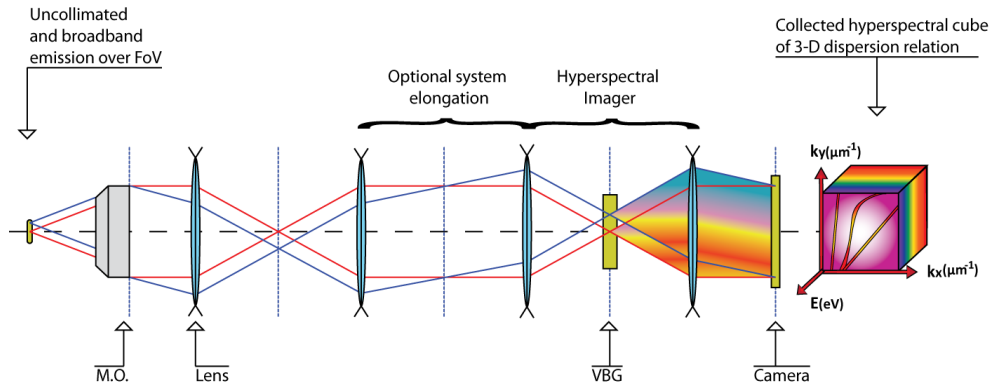


Figure 8. Hyperspectral setup for mapping of the SPR effect<sup>6</sup>. The integrated SPR microstructure is placed under a microscope objective (MO). The EM emissions from the sample are collimated by the MO and separated spectrally by a volume Bragg grating (VBG). The Fourier plane is then imaged onto a camera. The resulting measurements are 3D cubes of intensities distributed over the emitted energies and collected wavevectors

The measurements are carried out using the setup described in Fig. 8. We employed a Nikon CFI 60 Infinity-Corrected Brightfield M.O with N.A. = 0.3 that enabled us to collect a range of wavevectors,  $\mathbf{k}_{||} = \pm 0.3 \cdot k_0(\mathbf{E})$ , with  $\mathbf{E}$  being the set of emitted energies by the QW. The integration of the light intensities are made over the  $1\text{mm}^2$  grating and the PL of the substrate QW is emitting for a range of energies from 1.38 to 1.65 eV. A hyperspectral cross-section of a wavevector map at fixed  $E=1.476\text{eV}$  is shown in Fig.9 a). The local maxima of this cross-section, corresponding to diffracted SPs, are marked by white dots. The dotted black lines of Fig.7 a-b) are here superposed. When comparing the features of Fig. 7, we conclude that the distribution in wavevectors of the SPs intensity reproduces very well with the analytical predictions, where most of the collected signal comes from the diffracted SPs in the  $\pm 1^{\text{st}}$  orders. Also, it can be seen that the positions of the experimental peaks follow those predicted by the calculations. The asymmetric luminescent protuberance, visible around  $k_y=0.35\mu\text{m}^{-1}$  for all  $k_x$ , was observed for several substrates. We relate it to the misalignment in the hyperspectral system. The second generation system is expected to be free of this problem.

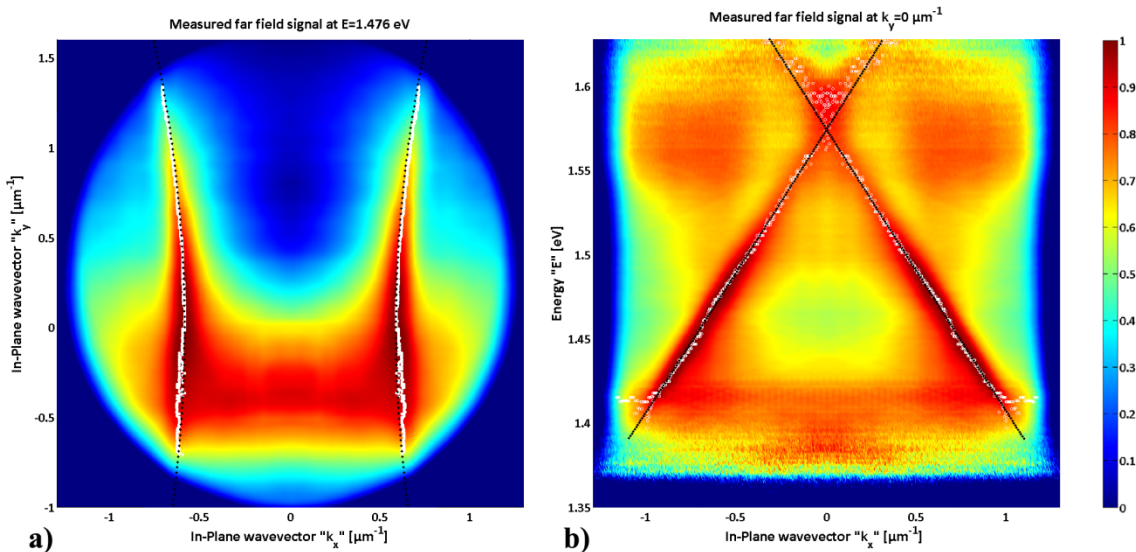


Figure 9 a) Measured  $(k_x, k_y)$  dispersion at 1.476 eV for the architecture presented in Fig.2. The dominant maxima are induced by the in-plane SPs. The dotted black lines are the analytical SPR peaks shown in Fig.7 while the white dots are the experimental local maxima. Fig.9 b) shows another cut at  $k_y = 0$  for all the energies emitted by the QW, showing a projected dispersion relation  $E(k_x)$ . Again, the dotted black lines are the analytical peaks presented in Fig.7 and the white dots, the experimental local maxima tracking the SPR. Both figures are in very good concordance with the calculations<sup>6</sup>.

Fig. 9 b) presents a different cross-section of the same measurement, this time at  $k_y=0$  for all the energies emitted by the QW microstructure. The local maxima are indicated by white dots and the black lines are those corresponding to the maxima predicted by the analytical calculations of Fig. 7 c-d). The projected dispersion relation of the device follows the analytical predictions of Fig. 7 very well, with the SPR diffraction as the dominant feature extracted for the far field emission. The signal is normalized for each energy, thus no standard PL curve is visible across Fig. 9 b), but decreased S/N is seen on the edges where the QW PL is weaker. The peak intensities, corresponding to SPR, can be tracked and monitored for an energy dependent surface sensing measurement. Within a single measurement, the complete  $E(\mathbf{k})$  dispersion for SPR can also be extracted in 3D, as presented in Fig. 10. This figure presents the extracted SPR peaks for the whole hyperspectral cube. The two diffracted SPR, from the  $\pm 1^{\text{st}}$  orders, are clearly visible. For the presented cube, each voxel has a resolution of  $[0.3 \cdot k_0(E)/1024 \mu\text{m}^{-1}, 0.3 \cdot k_0(E)/1024 \mu\text{m}^{-1}, k_0(E)^2 \cdot \hbar / 2\pi \cdot 10^{-9} \text{ eV}]$ , with cube size  $[0.3 \cdot k_0(E) \mu\text{m}^{-1}, 0.3 \cdot k_0(E) \mu\text{m}^{-1}, E \text{ eV}]$ , with  $E$  denoting the set of collected energies. It is important to mention that the resolution of the instrument is fully scalable by using different collecting objectives (the 0.3 factor) and camera units (the 1024 factor). Measurements reported here were carried out at room temperature and under relatively uncontrolled environmental conditions<sup>6</sup>.

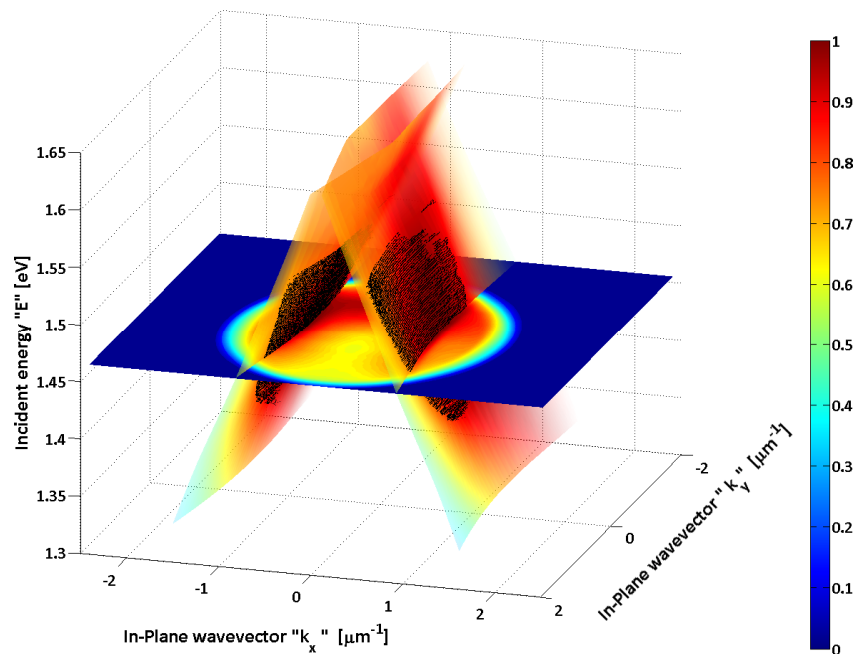


Figure 10 Measured SPR dispersion in  $I(E, k_x, k_y)$  for the integrated architecture presented in Fig. 2, as shown in literature<sup>6</sup>. The 3D SPR is extracted from the hyperspectral cube as local maxima, as exemplified by the black dots. The displacement of the 3D SPR in time should provide highly precise spectro-angular information on the biochemical perturbations within the SPs evanescent fields, typically between 100-200nm from the surface

It took 15 minutes to collect the cube shown in Fig. 10. This was achieved using a 2x2 binning on the camera and a 1s exposure time for each emitted energy. Faster and more precise measurements could be achieved with a stronger luminescent source that would allow reducing the binning and exposure time. The next challenge will involve the quasi real-time tracking of those SPR dispersion curves, in a 3D space, in order to accurately follow the spectroscopic SPR events taking place on the device surface.

## 6. CONCLUSIONS

The incorporation of the SPR technology in an integrated and portable total analysis system could be rendered possible through the use of light emitting semiconductor nanostructures. We have demonstrated a simple nano-SPR platform capable of coupling a multiplexed SPR signal in both wavevectors  $\mathbf{k}$  and energies  $E$ .

SPR on planar metal-dielectric interfaces is a multidimensional phenomenon with a spatially resolvable intensity expressed by  $I(E, k_x, k_y)$ . The embedment of a broadband light emitter in a substrate of a biosensing architecture allows one to fully take advantage of this phenomenon in a device where many energies are inducing SPR events for a continuum of planar wavevectors.

To accurately measure the photonic outputs of the proposed integrated GaAs-AlGaAs QW nanodevice, we introduced a hyperspectral measurement method. This enabled us to monitor the complete dispersion relations of the SPs and presents a novel way of acquiring massive amount of information related to light-scattering and direct mapping of the EM-wave induced phenomena. In the presented case, we showed the particular application for the measurement of SPR and tracking of the peak in a 3D space. The additional dimension of the SPR effect, measured with scalable resolution, allows increasing the precision of the tracking, reveals anisotropic surface interactions and provides spectroscopic response of the SPR effect.

Our future work will be oriented towards the further improvement of the experimental setup and acquisition methods in order to increase the precision, throughput and ease of access of the instrumentation. Sensitivity calibrations for biochemical agents will also have to be studied.

## 7. ACKNOWLEDGMENTS

The authors acknowledge the financial contribution from the Natural Science and Engineering Research Council of Canada (NSERC Strategic grant STPGP 350501 - 07), the Canada Research Chair in Quantum Semiconductors Program and the Vanier Canada Graduate Scholarship.

## REFERENCES

- [1] R. B. M. Schasfoort, and A. J. Tudos, [Handbook of surface plasmon resonance] Royal Society of Chemistry, Cambridge(2008).
- [2] H. Raether, "Surface-Plasmons on smooth and rough surfaces and on gratings," Springer Tracts in Modern Physics, 111, 1-133 (1988).
- [3] H. E. Debruijn, R. P. H. Kooyman, and J. Greve, "Surface-plasmon resonance microscopy - Improvement of the resolution by rotation of the object," Applied Optics, 32(13), 2426-2430 (1993).
- [4] B. Rothenhausler, and W. Knoll, "Surface-plasmon microscopy," Nature, 332(6165), 615-617 (1988).
- [5] S. J. Lee, and S. Y. Lee, "Micro total analysis system ( $\mu$ -TAS) in biotechnology," Applied Microbiology and Biotechnology, 64(3), 289-299 (2004).
- [6] D. Lepage, Jan J. Dubowski *et al.*, "Hyperspectral imaging of diffracted surface plasmons", Opt. Express, 18(26), 27327-27335 (2010).
- [7] D. Lepage, and J. J. Dubowski, "Surface plasmon effects induced by uncollimated emission of semiconductor microstructures," Opt. Express, 17(12), 10411-10418 (2009).
- [8] J. J. Burke, G. I. Stegeman, and T. Tamir, "Surface-polariton-like waves guided by thin, lossy metal films," Physical Review B, 33(8), 5186 (1986).
- [9] D. L. Mills, "Attenuation of surface polaritons by surface roughness," Physical Review B, 12(10), 4036 (1975).
- [10] A. Jimenez, D. Lepage, J. Beauvais *et al.*, "Quality of surfaces in the fabrication of monolithic integrated light source SPR system for bio-sensing purposes," Microelectronic Engineering, -To be published, (2010).
- [11] D. Lepage, A. Jimenez, D. Carrier *et al.*, "Plasmonic propagations distances for interferometric surface plasmon resonance biosensing," Nanoscale Research Letters, - To be published, (2011).
- [12] D. Lepage and Jan J. Dubowski, "Surface plasmon effects induced by uncollimated emission of semiconductor microstructures", Syn. and Photonics of Nano. Materials VII, 75860-7, Proceedings (2010)
- [13] L. F. Li, "Fourier modal method for crossed anisotropic gratings with arbitrary permittivity and permeability tensors," Journal of Optics a-Pure and Applied Optics, 5(4), 345-355 (2003).
- [14] L. Mashev, and E. Popov, "Reflection Gratings in Conical Diffraction Mounting," Journal of Optics-Nouvelle Revue d'Optique, 18(1), 3-7 (1987).
- [15] M. G. Moharam, D. A. Pommert, E. B. Grann *et al.*, "Stable implementation of the rigorous coupled-wave analysis for surface-relief gratings-enhanced transmittance matrix approach," Journal of the Optical Society of America a-Optics Image Science and Vision, 12(5), 1077-1086 (1995).

- [16] A. Giannattasio, and W. L. Barnes, "Direct observation of surface plasmon-polariton dispersion," *Optics Express*, 13(2), 428-434 (2005).
- [17] F. Romanato, K. H. Lee, H. K. Kang *et al.*, "Sensitivity enhancement in grating coupled surface plasmon resonance by azimuthal control," *Optics Express*, 17(14), 12145-12154 (2009).
- [18] S. Patskovsky, A. V. Kabashin, M. Meunier *et al.*, "Silicon-Based Surface Plasmon Resonance Sensing with Two Surface Plasmon Polariton Modes," *Appl. Opt.*, 42(34), 6905-6909 (2003).
- [19] P. Arudra, Y. Nguiffo-Podie, E. Frost *et al.*, "Decomposition of Thimerosal and Dynamics of Thiosalicylic Acid Attachment on GaAs(001) Surface Observed with in Situ Photoluminescence," *Journal of Physical Chemistry C*, 114(32), 13657-13662 (2010).
- [20] C. K. Kim, G. M. Marshall, M. Martin *et al.*, "Formation dynamics of hexadecanethiol self-assembled monolayers on (001) GaAs observed with photoluminescence and Fourier transform infrared spectroscopies - art. no. 083518," *Journal of Applied Physics*, 106(8), 83518-83518 (2009).